Published as S. Pargal, J. Yuan, and G. J. Brereton. J. Turbul., pages 1–27, 2021.

Impulse response of turbulent flow in smooth and riblet-walled channels to a sudden velocity increase

By S. Pargal, J. Yuan and G. Brereton†

This paper explores the use of a small-span direct numerical simulation for a transient, smooth-wall turbulent channel flow and then applies the small-span simulation to a transient channel flow with riblets. A flow configuration similar to that of S. He and M. Seddighi, *J. Fluid Mech.*, 715, 60–102 (2013) is used to study the impulse response of a half-height channel flow to an abrupt increase in bulk velocity (with a friction Reynolds number increasing from 180 to 418). A minimal domain span sufficient to include the near-wall quasi-streamwise vortices in the 'healthy turbulence' region is used. The turbulent flow undergoes reverse transition toward a quasi-laminar state, followed by a retransition phase to the new equilibrium state. On a smooth wall, detailed comparisons with a full-span case show that the small-span test case captures satisfactorily the essential dynamics during the entire transition process, although it yields a slight delay in recovery to the new equilibrium. This difference is attributed to a slower streak transient growth due to an underestimation of near-wall spanwise fluctuations. This underestimation is associated with the missing large attached eddies that are not contained in the small span of the simulation domain. These comparisons justify the use of small-span simulations for identifying the main flow physics in a non-equilibrium accelerating wall turbulence. The application to the riblet flow shows that riblets do not fundamentally affect the flow dynamics, but delay the retransition as a result of significantly milder streak meandering. The streak-stabilization effect of riblets is still active in a strongly accelerating turbulence and tends to prolong the flow recovery.

1. Introduction

1.1. *Turbulent flows over riblets*

Manipulating near-wall turbulent flows using active or passive control technique for drag reduction has been an intensive area of research in recent decades. As one example of passive flow control device, riblets are motivated by skin (dermal denticles) of fast-swimming sharks (Dean & Bhushan 2010). Drag reduction by riblets of up to 10% compared to a smooth wall has been widely demonstrated numerically and experimentally by, for examples, Walsh (1983), Bechert & Bartenwerfer (1989), Bechert *et al.* (1997), Choi *et al.* (1993), Lee & Choi (2008), Goldstein *et al.* (1995), and García-Mayoral & Jiménez (2011). Riblets have been shown to provide a 2% drag reduction during flight tests of an Airbus 320 when covering 70% of the aircraft surface (Szodruch 1991) Similar benefits were observed in flight tests by Boeing on airfoils with riblets (Mclean *et al.* 1987; Lee & Jang 2005; Raju & Viswanath 1998). Riblets have also been deployed on high speed trains (GEC 1991), racing swimsuits (Krieger 2004) and pipeline surfaces (Weiss 1993).

---

† Department of Mechanical Engineering, Michigan State University

Mechanisms of drag reduction have been studied for riblets with various two- or three-dimensional geometries (such as sawtooth, scalloped, trapezoidal, thin-blade shapes and shark skin moulding replicas), with the goal of optimizing drag reduction over a large Reynolds-number range. Bacher & Smith (1985), using flow visualization, observed that the transverse oscillation of low-speed streaks was reduced and the spanwise spacing between low-speed streaks was increased in the vicinity of riblets. This was hypothesized to reduce the effect of the local adverse pressure gradients induced by the hairpin vortices in provoking ejections near the wall (Smith *et al.* 1990). Using direct numerical simulations (DNS), Choi *et al.* (1993) found that the velocity fluctuations (in wall units) were weakened in drag-reducing riblet flows and proposed that the viscous drag is reduced by limiting the contact surface area of streamwise vortices, such that a smaller area is exposed to high-velocity fluid. Bechert & Bartenwerfer (1989) proposed the "protrusion height" concept, which was further improved by Luchini *et al.* (1991) and Bechert *et al.* (1997). It states that the virtual origin of the longitudinal flow is near the valley whereas that of the cross flow is lifted to around the riblet tip elevation, leading to increased shear stress of the cross flow, while hampering cross flow fluctuations and the spanwise transport. In addition, García-Mayoral & Jiménez (2011) noted that streamwise slip at the riblet tip augments velocity in the free stream and consequently leads to decrease of the friction coefficient. Rastegari & Akhavan (2019) carried out DNS analyses on super-hydrophobic surfaces and riblets, and observed that both types of surface share a common mechanism for drag reduction characterized by the effective slip velocity at the wall. For riblets with sizes larger than a threshold, the drag increases, associated with the appearance of quasi-two-dimensional spanwise vortices due to a Kelvin-Helmholtz-like instability (García-Mayoral & Jiménez 2011).

While the mechanism leading to drag modification was well discussed, most studies of flows over riblets have been carried out in equilibrium turbulent flows such as fully-developed channels and zero-pressure-gradient (ZPG) boundary layers. However, most practical turbulent wall flows are characterized by non-equilibrium temporal and/or spatial variations of the bulk flow. The goal of this study is to evaluate the effect of riblets in wall turbulence when subjected to a strong bulk-flow acceleration.

1.2. *Wall-bounded turbulence subjected to strong acceleration*

Strong flow accelerations are present in a wide range of engineering applications such as airfoils and turbine blades. In these flows, although the mean kinetic energy increases as a result of the acceleration, turbulence may become less vigorous and the flow may revert to a quasi-laminar state through a process called "quasi-laminarization" or "reverse transition" (Narasimha & Sreenivasan 1973; Launder 1964).

The mechanism of quasi-laminarization has been widely studied in smooth-wall turbulence, especially for spatial accelerations. McEligot & Eckelmann (2006) observed that the burst frequency is very sensitive to the acceleration, decreasing with the strength of acceleration. Bourassa & Thomas (2009) related such reverse transition processes to the stabilizing effects of acceleration on near-wall streaky structures caused by the decrease of the wall-normal and spanwise fluctuations, which have been shown to be responsible for the instability of streaks and near-wall vortices (Jiménez & Pinelli 1999*a*). Piomelli & Yuan (2013) and Yuan & Piomelli (2015) explained that such process is the result of diminished redistribution of turbulent kinetic energy (TKE) into wall-normal and spanwise fluctuations, as the pressure fluctuations rapidly decreases with the mean-flow acceleration. On the other hand, prevention of quasi-laminarization has been observed in flow over a rough wall, as the roughness augments the wall-normal and spanwise fluctuations, acting to oppose the stabilizing effect of acceleration.

Temporal accelerations of channel flows were studied by He & Seddighi (2013), He & Seddighi (2015) and Seddighi *et al.* (2015) in channel flows with and without roughness. In these studies, the flow was accelerated by rapidly increasing the mass flow rate over a very short time period. Evidence of stabilizing effects of acceleration was observed, including a decrease of friction coefficient and long streaky structures near the wall. As the flow recovered, turbulence spots were formed near the wall, which disturbed the stability of these long streaks, leading to their breakdown.

As a first step in studying the effects of riblets on an accelerating turbulent flow, we simulate a transient channel flow similar to that of He & Seddighi (2013) using DNS. Because of the relatively high cost of simulations of flow over riblets, we use a reduced spanwise domain size for the simulation, as part of the simulation approach described next.

1.3. *Minimal-span simulations*

The small size of a drag-reducing riblet (typically characterized with a spanwise wavelength of $o(10)$ times of the viscous length scale δ_ν or less) requires much higher spatial resolution in the spanwise direction than is required in a smooth-wall simulation. In addition, the ensemble averaging necessary for calculating statistics for temporally developing flows requires $o(10)$ times of repetition of the transient simulation with different initial conditions. To reduce the simulation cost while still resolving near-wall phenomena associated with the drag reduction, the minimal-span simulation of wall-bounded turbulence is employed.

Chung *et al.* (2015) and MacDonald *et al.* (2017*a*) carried out exhaustive analyses of small-span simulations using DNS and showed that simulations with a minimal spanwise length can capture near-wall dynamics, for both channel flows and half-height channel flows (termed “a half channel” hereafter), with the following constraints to accommodate minimal-flow units near the wall: (1) the spanwise domain length $L_z^+ > 100$; and (2) the streamwise domain length $L_x^+ > \max(1000, 3L_z^+)$. Here, + represents normalization by δ_ν and the friction velocity u_τ. If the wall is rough, the two additional constraints required to capture the essential flow structure in the vicinity of roughness: (1) $L_z > \lambda$, where λ is the characteristic spanwise wavelength of the rough surface; and (2) the roughness crest height $k_c < 0.4L_z$.

MacDonald *et al.* (2017*b*) showed that the near-wall dynamics were captured adequately in riblet flows in both drag-reducing and drag-increasing cases in fully-developed channels with small spans; a $L_z^+ = 120$ was used to include 4-8 riblet units. The cost effectiveness of the minimal-span approach was analyzed by MacDonald *et al.* (2017*a*), who found that a pyramid roughness requires 20 times less CPU time in minimal-span simulations when compared to full-span ones.

1.4. *Objectives*

The objectives of this work are two-fold: (1) to evaluate the capability of a small-span simulation for smooth-wall turbulence in a transient half channel, to address the question of how the missing large-scale outer-layer motions affect the near-wall response; and (2) to compare the results of small-span simulations of transient half channel flows bounded by a smooth wall and a riblet-covered wall, to identify the riblet effect under transient acceleration.

In Section 2, the problem set-up, numerical techniques, and details of the riblets used are introduced. Section 3.1 focuses on the initial rapid acceleration stage (i.e. stage during the 'impulse' jump of bulk velocity) of the smooth-wall flow and develops an analytical solution of the mean velocity, which is then compared with DNS observations. The turbulence response after the velocity jump is then analyzed in Section 3.2, by comparing small- and full-span flows on the smooth wall, and in Section 3.3, by comparing small-span flows on smooth and riblet-covered walls.

2. Problem formulation

2.1. *Governing equations*

The incompressible flow of a Newtonian fluid is governed by the equations of conservation of mass and momentum:

$$\frac{\partial u_i}{\partial x_i} = 0, \tag{2.1}$$

$$\frac{\partial u_j}{\partial t} + \frac{\partial u_i u_j}{\partial x_i} = -\frac{\partial P}{\partial x_j} + \nu \nabla^2 u_j + F_j. \tag{2.2}$$

Here, x_1, x_2 and x_3 (or x, y and z) are, respectively, the streamwise, wall-normal and spanwise directions, and u_j (or u, v and w) are the velocity components in those directions. t is time, $P = p/\rho$ is the modified pressure, ρ the density and ν the kinematic viscosity. The term F_j in Equation (2.2) is a body force per unit mass prescribed by an immersed boundary method (IBM) to impose no-slip boundary condition on the riblet surface, whose geometry is well-resolved by the grid (further details provided in Sec 2.3). The IBM method is based on the volume-of-fluid approach; its detailed implementation and validation are provided in Yuan & Piomelli (2014*b*,*a*). The values of F_i are either negligibly small or zero except in the fluid-solid interface cells. The simulations are performed using a well-validated code that solves the governing equations (2.1) and (2.2) on a staggered grid using second-order, central differences for all spatial derivatives, second-order accurate Adams-Bashforth semi-implicit time advancement, and MPI parallelization (Keating *et al.* 2004).

To obtained turbulent statistics for the transient flow simulations, ensemble averaging is performed at each point in time. When riblets are present, ensemble-averaged variables are spatially heterogeneous near the wall. These spatial fluctuations of the mean fields (also termed form-induced fluctuations) are separated from turbulent fluctuations using the double-averaging (DA) decomposition introduced by Raupach & Shaw (1982),

$$\theta(\vec{x}, t) = \langle \overline{\theta} \rangle (y, t) + \overline{\theta}''(\vec{x}, t) + \theta'(\vec{x}, t), \tag{2.3}$$

where θ is an instantaneous flow variable, $\langle \theta \rangle$ is the intrinsic spatial average in the (x, z)-plane, $\langle \rangle = [1/A_f] \int_{A_f} () \, dA$ (where A_f is the area occupied by fluid), $\overline{\theta}$ is the ensemble average, $\theta' = \theta - \overline{\theta}$ is the instantaneous turbulent fluctuation, and $\overline{\theta}'' = \overline{\theta} - \langle \overline{\theta} \rangle$ is the form-induced fluctuation. In addition, the area averaging carried out in the total (x, z)-plane area of fluid and solid, $A_o = L_x L_z$, is termed superficial area averaging, denoted by $\langle \rangle_s = [1/A_o] \int_{A_f} () \, dA$ and L_{x_i} is the domain size in the x_i direction. The two area averaging approaches satisfy the relation $\langle \rangle_s = \Phi(y) \langle \rangle$, where $\Phi(y)$ is the area fraction of fluid in the (x, z)-plane at elevation y, or the "roughness geometry function" (Nikora

Case	Wall	Span	Re_{b1}	Re_{b2}	$Re_{\tau 1}$	$Re_{\tau 2}$	L_z/δ	Δx^+	$\Delta y^+_{\rm min}$	$\Delta y^+_{\rm max}$	Δz^+
SF	Smooth	Full	2825	7404	180	418	3.5	4.5-10.0	0.2-0.56	3.5-8.3	2.5-6.5
SS	Smooth	Small	2921	7581	180	418	1	4.5-10.0	0.2-0.56	3.5-8.3	2.5-6.5
RS	Riblet	Small	2833	7383	180	418	1	4.5-10.0	0.2-0.56	3.5-8.3	0.47-1.0

TABLE 1. Simulation parameters. $L_x/\delta = 12.8$ and $L_y/\delta = 1.0$ for all cases.

et al. 2007),

$$\Phi(y) = \frac{A_f(y)}{A_o}. \tag{2.4}$$

In this paper, for the quantities that are defined in fluids only—such as velocities, pressure, stresses—either intrinsic or superficial averaging is carried out. Note also that, for smooth-wall simulations, the $\overline{\theta}''$ component is zero. The wall shear stress is determined by integrating the ensemble-averaged streamwise IBM body force F_1,

$$\tau_w(t) = \frac{\rho}{L_x L_z} \int_{\mathcal{V}} \overline{F_1}(\vec{x}, t)\, \mathrm{d}x\mathrm{d}y\mathrm{d}z, \tag{2.5}$$

where $\mathcal{V}$ represents the total simulation domain. For a detailed explanation of this method, see Yuan & Piomelli (2014*a*). The method in Eq. (2.5) was validated by Yuan & Piomelli (2014*b*) in the case of a fully developed channel flow with sandgrain roughness; the same simulation methodology was employed therein. The validation was carried out by comparing τ_w from Eq. (2.5) to the total shear stress at $y = 0$ (valley of roughness) obtained from mean momentum balance. Very good agreement was obtained. As another validation specifically for the use of this method in riblet-wall flows, the roughness function in the final steady state is shown to compare very well with the experimental measurements of Bechert *et al.* (1997) in Sec. 3.3.

2.2. *Simulation parameters*

For the transient channel simulations, the setup is similar to the one used by He & Seddighi (2013). Specifically, the channel flow is forced by the streamwise pressure gradient, with periodic boundary conditions applied in x and z, and symmetric boundary condition at the top boundary as only a half channel is simulated. The temporal flow acceleration is achieved by imposing a temporally varying streamwise pressure gradient, which is adjusted at each time step to produce the prescribed rapid linear increase of the bulk velocity from u_{b1} to u_{b2} over the transient time interval $t^* = tu_{\tau 1}/\delta = 0$ to $t^* = 0.005$, after which the bulk velocity is kept constant. Here δ is the channel half height.

The simulation parameters are summarized in Table 1 for all cases. Each case name contains two capital letters: the first letter represents the wall type (S for smooth and R for riblet) and the second denotes the domain span (F for full span and S for small span). For case SF (full span simulation on the smooth wall), the initial and final bulk Reynolds numbers are $Re_{b1} = U_{b1}\delta/\nu = 2825$ and $Re_{b2} = 7404 \approx 3Re_{b1}$ and the time dependence of Re_b is shown in Figure 1(a). The friction Reynolds numbers Re_τ are 180 and 420 for the initial and final states, respectively and Δx_i is the grid size in the x_i direction.

For the ensemble averaging, multiple transient simulations with uncorrelated initial conditions were performed for each case. The procedure is detailed as below. For each case, first the fully-developed half-channel flows at Re_{b1} for the corresponding configu-

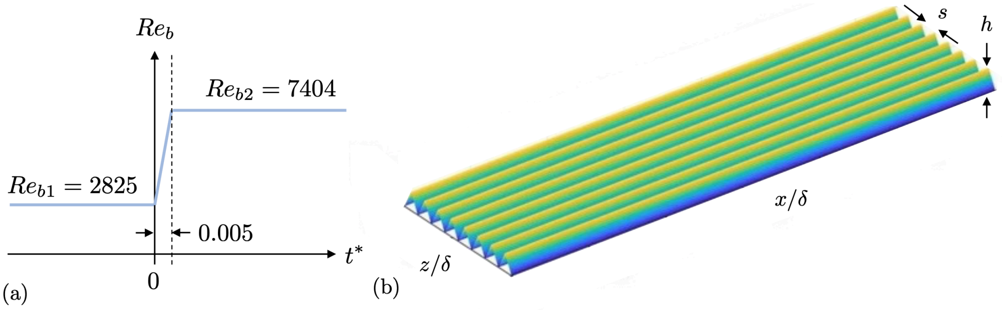

FIGURE 1. (a) Prescribed Re_b variation in time for case SF; $t^* = tu_{\tau 1}/\delta$. (b) Sawtooth riblets with $h/\delta = 0.042$ and $h/s = 1$, where h and s are riblet height and spacing; a fraction of the domain is shown (1/8 in x and 1/2 in z).

rations (including span and wall type) were simulated. From these initial simulations, data were collected for a duration of 200 and 400 large-eddy turn-over time (LETOT or δ/u_τ), for the full- and small-span cases respectively, after the simulations had dynamically converged. Within these flow data at Re_{b1}, 34 and 20 equally spaced snapshots, for the riblet- and smooth-wall cases respectively, were used as different initial conditions for the transient simulations. The transient simulations were then carried out until the new steady state is reached for first- and second-order velocity statistics converged. The convergence of ensemble averages was demonstrated by the observation that using half the number of separate transient simulations for ensemble averaging led to a change of up to 1% in $U \equiv \langle \overline{u} \rangle$ and 4% in $\langle \overline{u'^2} \rangle$.

Previous studies of small-span simulations for fully-developed channels showed that the mean flow and statistics of velocity fluctuations were reproduced accurately in the near-wall region corresponding to y/L_z less than 0.3 to 0.4 (MacDonald *et al.* 2017*a*; Flores & Jiménez 2010; Hwang 2013)—the region of “healthy turbulence” as defined by Flores & Jiménez (2010). Above this region the mean velocity profile in wall units, $U^+(y)$, showed an upward shift compared to full-span simulations and the streamwise and wall-normal velocity fluctuations were enhanced for full-height channel flows. Changing to a half-height channel configuration for the minimal span simulations had a negligibly small effect on statistical measures in the healthy turbulence region, but was found to dampen streamwise fluctuations far from the wall (MacDonald *et al.* 2017*a*). Most of the changes caused by the reduced span were attributed to the absence of eddies larger than $0.4L_z$.

For the reason discussed above, in these steady-state small-span simulations the friction velocities were reproduced accurately, but the bulk velocities were systematically overpredicted. The flow acceleration transient used herein was therefore a prescribed increase in $Re_\tau = u_\tau \delta/\nu$, rather than Re_b. Specifically, separate small-span simulations of fully-developed half channels were carried out at the two Re_τ values to evaluate the corresponding “overpredicted” values of u_{b1} and u_{b2} to be imposed in order to achieve the $u_{\tau 1}$ and $u_{\tau 2}$ values that matched the friction velocities in full-span simulations. The corresponding “overpredicted” Re_{b1} and Re_{b2} values were then used to enforce the desired acceleration transient in the small-span simulations.

For the small-span simulations, a spanwise domain length of $L_z/\delta = 1$ was used rather than the full-span value of 3.5. The chosen length of $L_z/\delta = 1$ is equivalent to $180 < L_z^+ < 418$ in these simulations and is significantly larger than the smallest allowable value proposed in the literature for equilibrium wall turbulence, of $L^+_{z,\min} = 100$. The L_z/δ

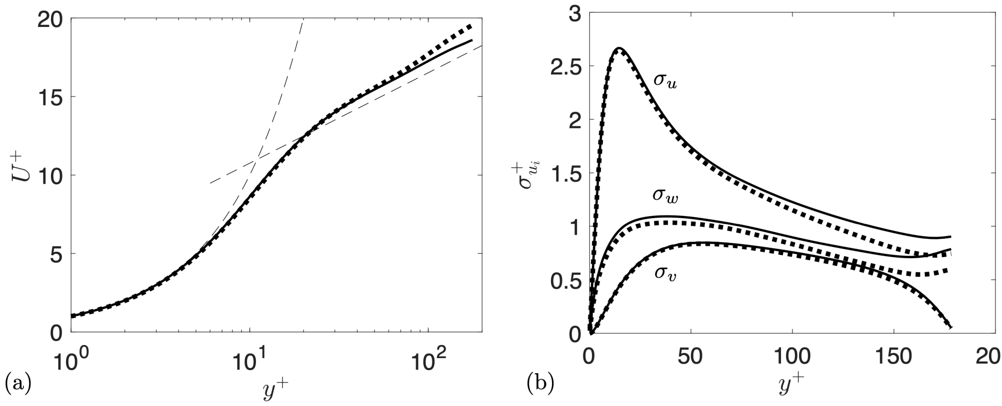

FIGURE 2. (a) Streamwise mean velocity and (b) rms velocity fluctuations normalized by wall units in the initial steady state, for full- (———) and small-span (- - -) smooth-wall cases (SF and SS). In (a), thin dashed lines are $U^+ = y^+$ and $U^+ = (1/4.0)\log y^+ + 5.0$.

value was selected for the following reason. In a strongly accelerating flow, the near-wall cycle of turbulence generation involving low-speed streaks and quasi-streamwise vortices is modified (discussed in Sec. 3.2.2). Therefore, if the small-span simulation is to capture the variation of crucial aspects of the near-wall dynamic cycle, it may be necessary to choose the value of L_z such that the quasi-streamwise vortices are contained (statistically speaking) inside the healthy turbulence region (i.e. $y/L_z < 0.4$). The wall-normal extent of quasi-streamwise vortices are generally considered to be below $y^+ = 50-70$ on average, as, for example, shown by the velocity spectral analysis of Hwang (2015) and the eddy eduction of Jeong *et al.* (1997). Enclosing the region of $y^+ < 70$ inside the healthy turbulence region would require $L_z^+ \geq 175$. This requirement is satisfied for both the initial and final equilibrium states when $L_z/\delta \approx 1$. The same value of L_z/δ was used for smooth-wall and riblet cases of small-span simulations, as riblets do not appear to modify significantly the size of near-wall vortices.

The streamwise domain size, $L_x/\delta = 12.8$, was chosen to be the same for both small- and full-span simulations to accommodate near-wall streaky structures, which are known to be elongated well past 1000 wall units during acceleration. In Sections 3.2.1 and 3.3 we show that the elongation of flow structure also occurs in the small-span cases. The L_x/δ value is the same as used by He & Seddighi (2013).

The grid sizes were chosen based on the critical stage of the transient flows—the final state—where Re_τ is higher than the initial state. The grid spacing is uniform in x and z, whereas, for y, the grid is stretched with a finer resolution near the wall. For the smooth-wall cases, the numbers of grid points are $512 \times 300 \times 256$ in x, y and z for a full-span simulation and $512 \times 300 \times 64$ for a small-span one.

The full-span smooth-wall simulation has been validated against the results of Kim *et al.* (1987). Figure 2 compares the flow statistics between the two smooth-wall cases with small and full spans. The small-span simulation yields an upward shift in the $U^+(y)$ profile for $y/L_z > 0.4$ and slightly lower $\langle \overline{u'^2} \rangle^+$ far from the wall. Values of $\langle \overline{w'^2} \rangle^+$ are also smaller throughout the channel. These observations are consistent with those of MacDonald *et al.* (2017*a*) from their half-channel simulations with minimum spans. The weaker spanwise fluctuations near the wall appear to impact quantitatively the transient process, as will be discussed in Sec. 3.2.2. MacDonald *et al.* (2017*a*) observed that the minimal span augments $\langle \overline{v'^2} \rangle^+$ far from the wall for a half channel. This is, however, not the case for the present small-span simulation, perhaps due to a significantly lower Reynolds number ($Re_{\tau 1} = 180$, compared to 600 in the study of MacDonald *et al.* (2017*a*)).

2.3. *Simulations with riblets*

As the sawtooth-type riblet is among the most widely studied geometries in the literature, we choose this geometry. The riblet wall simulated herein is shown in Figure 1(b). h and s represent the height and width (or spacing) of a riblet unit, respectively. For this type of riblets, existing studies (for references see Sec. 1.1) showed that (1) a height-width ratio of $h/s \approx 1$ give higher drag reduction in comparison to other ratios and (2) a drag-reducing regime requires $h^+ \leq 25$. In this work, h/s is set to 1. As the flows are intended to be drag-reducing, we set $h/\delta = 0.042$, which yields h^+ values of 7.5 and 17.5 in the initial and final equilibrium states, respectively.

Small-span simulations are carried out for the flow over riblets with a L_z containing 24 riblets, each resolved by 16 grid points in the z direction. In existing DNS studies of flows over riblets, between 8 and 32 grid points per riblet in z were used (Choi *et al.* 1993; Goldstein *et al.* 1995; Goldstein & Tuan 1998). Note that in the work of Choi *et al.* (1993) a body-fitted mesh was used, while in the present study an immersed boundary method was employed. As such, the spatial resolution quantified by the number of grid points per riblet are not directly comparable. Nevertheless, the present resolution falls in the range used in the literature. We have also validated the resolution by comparing single-point velocity statistics with the benchmark case of Choi *et al.* (1993) for a fully-developed riblet-wall channel flow simulation (not shown herein). The origin of the y axis is imposed at the trough of each riblet. Below the riblet tip (at $y = h$), a uniform y grid is used with $\Delta y/h = 0.0032$ or $\Delta y^+ = 0.24$ and 0.56 in the initial and final states respectively. The total number of grid points for case RS is $512 \times 300 \times 384$ in x, y, and z. In Section 3.3 it is shown that the present calculated drag reduction in the new equilibrium state compares very well with the experimental measurement of Bechert *et al.* (1997) with the same riblet configuration, serving as a validation for the riblet simulations.

The following additional conditions apply for small-span simulations with riblets: (1) $h/L_z < 0.4$ since essential flow physics is resolved only for $y < 0.4L_z^+$, according to Chung *et al.* (2015); and (2) $h/\delta < 0.15$, i.e. riblet tips do not protrude into the outer layer, to ensure the existence of a logarithmic region in the equilibrium states. Since the riblets are very small compared to δ to achieve drag reduction for both $Re_{\tau 1}$ and $Re_{\tau 2}$, these requirements were both satisfied.

3. Results and Discussion

3.1. *Flow response during the forcing transient*

The imposed change in u_b shown in Figure 1(a) follows the well-defined analytical form of a linear increase, in a spatially fully-developed flow. It lasts only 0.0053 large-eddy turn-over time (or 0.9 viscous time units, ν/u_τ^2), which is several orders of magnitude shorter than the integral time scale, and so the energy-containing turbulence field during the transient may be assumed ‘frozen’ at its state at the beginning of the transient. If the x-z planar average of the streamwise velocity $U(y,t)$ is decomposed into the sum of an initial and a transient component, as $U(y,t) = U(y,t_0) + \widetilde{U}(y,t)$, where t_0 is the time at which the transient velocity increase begins, an x-momentum equation describing the

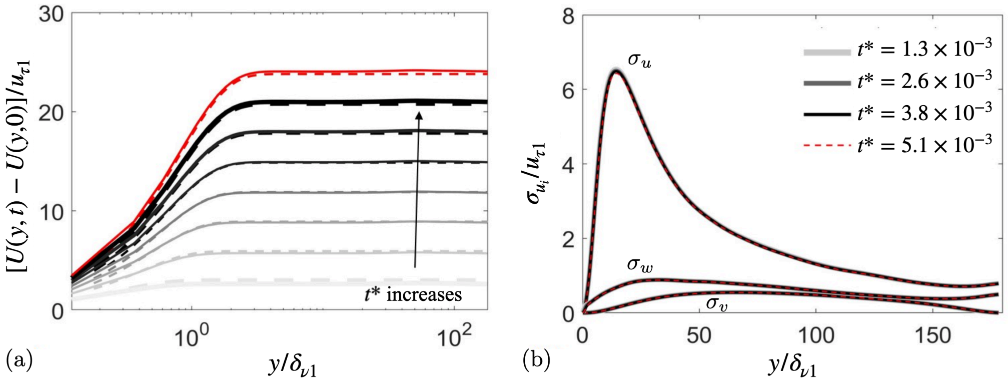

FIGURE 3. Variation of (a) mean velocity with respect to its initial state, normalized by initial friction velocity (arrow showing increase in t^*=6.4e-4 (light gray) to 5e-3 (red)) in comparison with analytical results(- - -) (b) Velocity rms fluctuations with respect to initial friction velocity during acceleration.

evolution of the transient velocity component can be written as

$$\frac{\partial \widetilde{U}}{\partial t} = -\frac{1}{\rho}\frac{d\widetilde{P}}{dx} + \nu\frac{\partial^2 \widetilde{U}}{\partial y^2}, \tag{3.1}$$

where $\widetilde{P}$ is the corresponding transient pressure. For the case of a time-linear transient in flow rate in a fully-developed channel flow, an exact solution to Eq. (3.1) can be found.

Eq. (3.1) can be solved by Laplace transforming it, solving the resulting ordinary differential equation analytically, and applying boundary conditions of no slip and symmetry at the channel wall and center respectively. The resulting expression for the transformed velocity $\widehat{U}(y,s)$ (where s is the transform-domain variable) is then integrated with respect to y to yield a relationship between the transformed transient pressure gradient and flow rate (which is specified as αt or, in the transform domain, α/s^2). The transformed pressure gradient is then substituted into the solution for $\widehat{U}(y,s)$ to yield the exact solution:

$$\frac{\widetilde{U}h}{\nu} = \frac{\alpha\delta^3}{\nu^2}\,\mathcal{L}^{-1}\left\{\left[\frac{\nu}{\delta^2 s}\right]^2\left[\frac{\cosh(\xi\,[1-y/\delta]) - \cosh(\xi)}{\sinh(\xi)/\xi - \cosh(\xi)}\right]\right\}\frac{\delta^2}{\nu}, \tag{3.2}$$

where $\xi = \sqrt{s/\nu}\delta$ and $\mathcal{L}^{-1}$ denotes the inverse Laplace transform. The transform-domain equations used in this derivation are given for transients of arbitrary time dependence as Eqns. (7) and (8) in Brereton (2000).

For the particular case of very short times, the argument of the inverse transform in Eq. (3.2) can be expanded for large s as

$$\mathcal{L}^{-1}\left\{\left[\frac{\nu}{\delta^2 s}\right]^2\left[1 - e^{-\xi[1-y/\delta]}\right]\right\},$$

which can be inverse transformed directly, with the result that

$$\frac{\widetilde{U}\delta}{\nu} = \frac{\alpha\delta^3}{\nu^2}\int_0^p \operatorname{erf}\left\{\frac{y/\delta}{2\sqrt{p}}\right\} dp, \quad \text{where} \quad p = \nu t/\delta^2\ . \tag{3.3}$$

This analytical solution for the transient velocity $\widetilde{U}(y,t) = U(y,t) - U(y,t_0)$ is plotted in Figure 3(a) together with the corresponding DNS data for smooth-walled channel flow, as profiles at each of 8 equally spaced intervals within the transient. The corresponding time-dependent behavior of profiles of the DNS-determined root-mean-square velocity fluctuations σ_u, σ_v, and σ_w are shown in Figure 3(b). In this figure, no discernible time dependence can be seen in the stresses; so the assumption of frozen turbulence appears to be justified. The very good agreement between the analytical and DNS velocity profiles is consistent with the observation of frozen turbulence and indicates that the numerical forcing technique produced the desired velocity transient without spurious effects.

A comment is provided here regarding the spatial resolution during the abrupt transient. The discussion of sufficiency of grid resolution in Sec. 2.2 was for steady flows only. During the short abrupt transient, however, u_τ drastically increases (as will be discussed in Sec. 3.2) and the spatial resolution reduces to $\Delta y^+_{\rm min} \approx 1$ at the end of the impulse acceleration. As such, the flow response during the very short time period after $t^* = 0$ is not as accurately captured as in the steady states. However, as u_τ decreases rapidly after the abrupt acceleration and stays equal to or below $u_{\tau 2}$ for $t^* > 0.05$ (shown in Fig. 4 later), the resolution is sufficient for the majority of the transient process, which lasts for a period of $\Delta t^* \approx 1.5$. The suitability of the grid for resolving the flow during the abrupt transient is assessed here by examining how closely the computed velocity field matches the quasi-laminar analytical solution for transient flow, during which the turbulence is ‘frozen.’ The very good agreement implies that the grid is satisfactory for the main response during the abrupt transient. The slight discrepancy between DNS and analytical results may be attributed to the temporarily reduced resolution.

The response of the mean flow during the forcing transient is a quasi-laminar one, with negligibly small changes in the turbulence field. Furthermore, the transient viscous shear or Stokes layer at the surface penetrates only to about $y^+ = 4$ by the end of the transient and the increased shear within this layer does not appear to have caused any measurable change in the turbulence field by the end of the transient. The outer-flow velocity increase is uniform in the y-direction at all times within the transient. Because of its uniformity, there is no change in the local velocity gradient or in turbulence production terms and so the flowfield during the transient is a superposition of a linearly accelerating slug flow on the initial equilibrium turbulent boundary layer. Therefore, with the exception of the thin Stokes layer, the effect of this mean-flow forcing approaches that of a step change in velocity over the entire flow with a frozen turbulence field—an ideal transient for which to study the impulse response of the flow. This response begins after the end of the transient, when the Stokes layer penetrates further from the wall and the entire flow begins its adjustment to the newly imposed velocity field. It is described in detail below.

3.2. *Transient flow in the smooth-wall channel*

In the following, the smooth-wall cases with full and small spans (cases SF and SS) are compared, to establish how effectively the small-span simulation is able to capture the main flow characteristics.

3.2.1. *Turbulent statistics and structure*

Figure 4 compares the variation of friction velocity between the full- and small-span cases. The curves all start from $u_\tau/u_{\tau 1} = 1$ at $t^* = 0$ (though this data point is not seen in Fig. 4 as it is outside the axis range), followed by a sudden increase in $u_\tau/u_{\tau 1}$ (to as large as 8.7 at the end of the impulse acceleration) due to the increase in the bulk

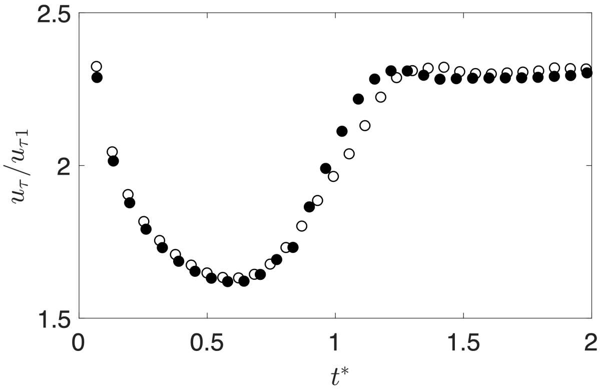

FIGURE 4. Variation of friction velocity with time for full- (filled symbols) and small-span (open symbols) smooth-wall cases. u_τ is normalized using initial friction velocity,

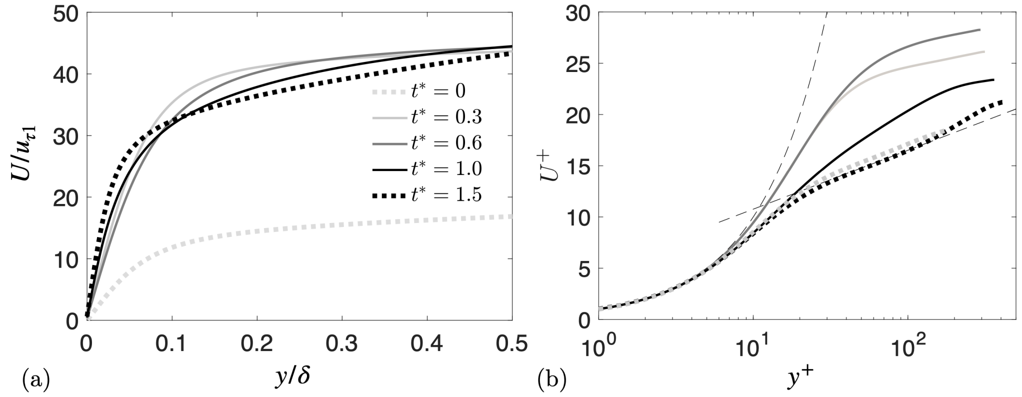

FIGURE 5. Streamwise mean velocity versus y for full-span smooth case: (a) linear plot with normalization in initial u_τ and δ and (b) semi-logarithmic plot with normalization in instantaneous wall units. In (b), thin dashed lines are $U^+ = y^+$ and $U^+ = [1/4.0] \log y^+ + 5.0$.

velocity. Following this, two stages of transition can be seen: (1) reverse transition toward the quasi-laminar state, with a decrease of friction coefficient (or in our case a decrease of $u_\tau/u_{\tau 1}$), and (2) re-transition, the onset of which is defined as the start of the increase in $u_\tau/u_{\tau 1}$, following He & Seddighi (2013). The main difference between the two cases appears to be a delay in reaching the final equilibrium state for the small-span case. In the reverse transition phase, only very slight differences are observed (up to 1.5%), which is possibly due to data sampling. The onset of the re-transition does not appear to be affected by the use of the small domain span.

Figures 5-7 show the time variation of the mean flow and Reynolds stresses. Since the main flow features of the full- and small-span cases are very similar, for brevity Figures 5-6 contain only results for the full-span case, while Figure 7 shows comparisons between the two.

The linear plot of the mean velocity U in case SF, normalized by the initial u_τ ($u_{\tau 1}$), is shown in Figure 5(a), compared to U normalized by the instantaneous $u_\tau(t)$ against the logarithm of y^+ in Figure 5(b). The U magnitude undergoes a rapid increase immediately after $t^* = 0$ to almost three times of the original magnitude, with a much stronger mean

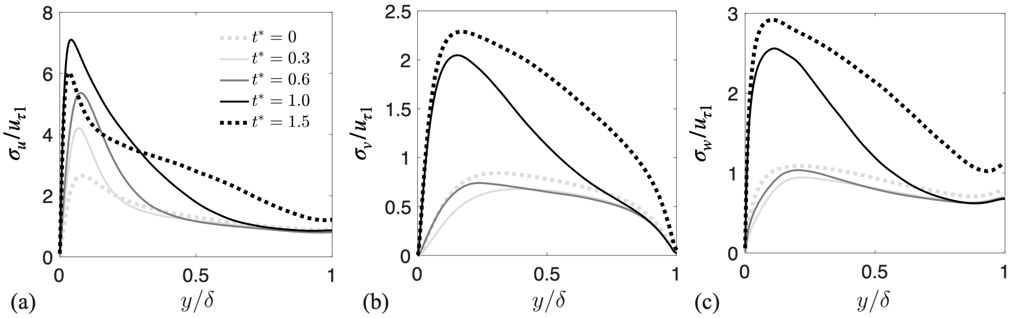

FIGURE 6. Velocity rms fluctuations in (a) the streamwise, (b) wall-normal and (c) spanwise directions for full-span smooth case.

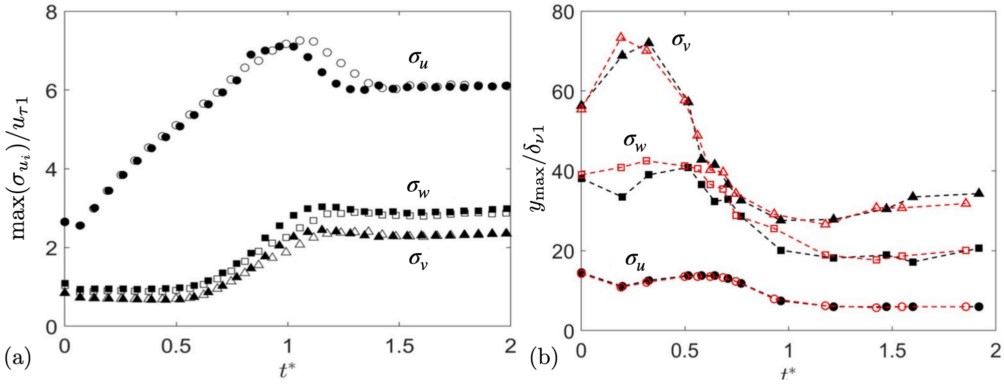

FIGURE 7. Temporal variation of (a) peak values and (b) peak elevations of rms velocity fluctuations for full- (filled symbols) and small-span (open symbols) smooth cases.

shear, $\partial U/\partial y$, near the wall (shown at $t^* = 0.3$), compared to the initial state at $t^* = 0$. After the onset of retransition, the U profile becomes flatter with slightly increased shear at the wall, as the flow starts to recover to a new fully-turbulent state, which is achieved at $t^* = 1.5$. Early in the transient, the near-wall $U^+(y)$ profile displays a thicker near-wall region in which a laminar law-of-the-wall ($U^+ = y^+$) is followed, indicating reverse transition of the near-wall flow.

Figure 6 shows the temporal development of turbulent fluctuations in case SF. In the reverse-transition stage, the magnitude of streamwise fluctuations, normalize by $u_{\tau 1}$, increases steadily near the wall as a consequence of stronger shear production. At the same time, wall-normal (σ_v) and spanwise (σ_w) rms fluctuations are slightly damped. It is also shown in Figure 7(a) by the time-variation of rms peak values. Figure 7(b) shows the variation of rms peak elevations. During much of the reverse transition stage, the peaks (especially for σ_v) move farther from the wall as the viscous sublayer thickens. During retransition, turbulent spots promote growth of σ_v and σ_w toward the new equilibrium and shift the rms peaks toward the wall due to the new, higher-Reynolds-number turbulence (He & Seddighi 2013). Specifically, the σ_v peak starts to move toward the wall at $t^* \approx 0.3$, followed by the inward movements of σ_w peak at around $t^* \approx 0.5$, just before the onset of retransition, as identified by the $u_\tau(t)$ profile. The σ_u peak starts to move towards the wall at $t^* \approx 0.7$. Also, Figure 7(a) shows overshoots in the peak values of all components before they reach their final state.

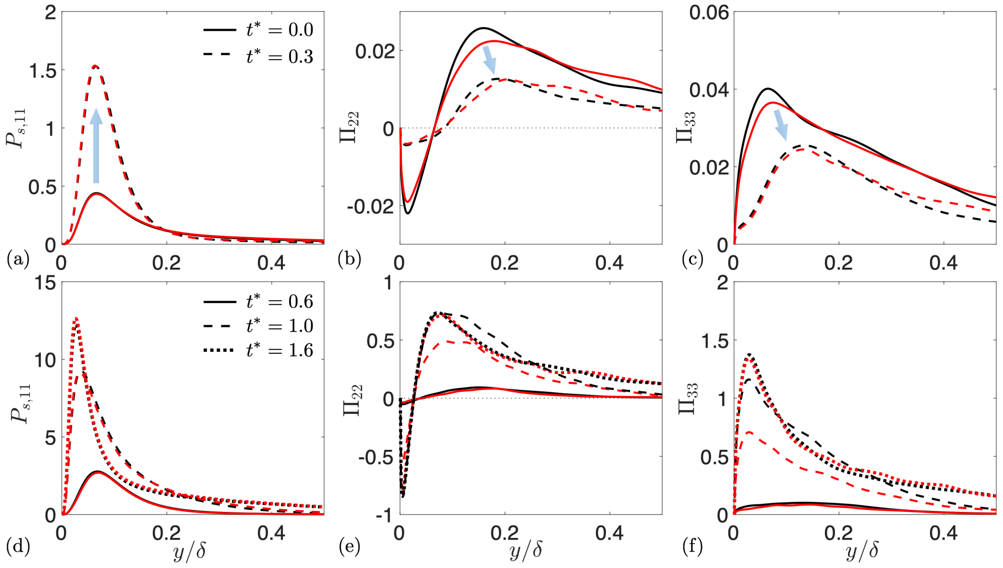

FIGURE 8. Selective Reynolds stress budget terms for full- (black) and small-span (red) cases: (a,d) Shear production of $\langle\overline{u'^2}\rangle_s$, (b,e) pressure strain of $\langle\overline{v'^2}\rangle_s$ and (c,f) pressure strain of $\langle\overline{w'^2}\rangle_s$, normalized by $u_{\tau 1}^4/\nu$, in (a-c) reverse-transition stage and (d-f) retransition stage.

The variations in small- and full-span cases in Figure 7 are very similar. The differences between the two cases are: (i) slightly lower peak values of σ_w in the equilibrium states; (ii) slower increase of turbulence intensity in v' and w'; and (iii) a delayed establishment of the new equilibrium state, for the small span case. The shapes of the rms profiles are very similar during the entire process for both cases. The wall-normal locations (Figure 7(b) of the peak-fluctuations compare well too.

To explain the slower turbulence response in the small-span case, the Reynolds stress budgets are discussed. The budget equation for the $\alpha\alpha$ component of the Reynolds stress tensor for a smooth-wall channel flow is (no summation over Greek indices)

$$\frac{\partial}{\partial t}\langle\overline{u'_\alpha u'_\alpha}\rangle_s = \underbrace{-2\langle\overline{u'_\alpha v'}\rangle\frac{\partial\langle\overline{u}_\alpha\rangle_s}{\partial y}}_{P_{s,\alpha\alpha}} - \frac{\partial}{\partial y}\langle\overline{u'_\alpha u'_\alpha v'}\rangle_s \underbrace{-2\left\langle\overline{P'\frac{\partial u'_\alpha}{\partial x_\alpha}}\right\rangle_s}_{\Pi_{\alpha\alpha}}$$

$$-2\frac{\partial\langle\overline{P'u'_\alpha}\rangle_s}{\partial x_\alpha} + \nu\frac{\partial^2}{\partial y^2}\langle\overline{u'_\alpha u'_\alpha}\rangle_s - \epsilon_{\alpha\alpha}. \tag{3.4}$$

The first and the third terms in Equation (3.4) are the shear production and the pressure strain term, respectively. $P_{s,11}$ is the only source of TKE generation, while Π_{22} and Π_{33} redistribute TKE to v' and w' motions. The variations of these three terms are compared between the two cases in Figure 8. For the full-span case, the peak of $P_{s,11}$ monotonically increases from the acceleration at $t^* = 0$ due to the constant, more intense mean shear at the wall, till the new equilibrium is reached at $t^* \approx 1.5$. In contrast, Π_{22} and Π_{33} decrease significantly near the peak elevations for $t^* = 0 - 0.3$, consistent with the findings for a spatially accelerating boundary layer (Piomelli & Yuan 2013). After the onset of retransition at $t^* \approx 0.6$, Π_{22} and Π_{33} rapidly increase and reach a quasi-equilibrium state at $t^* \approx 1.0$ well before the new equilibrium state is reached (at

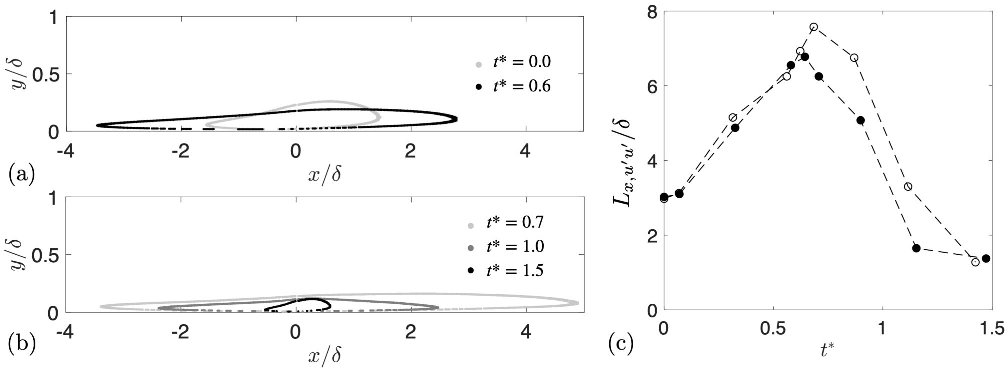

FIGURE 9. $R_{uu}(r_x, r_y)$ in (a) reverse-transition stage, centered at $y/\delta_{\nu 1} \approx 15$, and (b) retransition stage, centered at $y/\delta_{\nu 2} \approx 15$, for the full-span smooth case. (c) Variation of x-extent of $R_{uu} = 0.3$ isocontour in time, for both full- (filled symbols) and small-span (open symbols) smooth cases.

$t^* \approx 1.5$). Although progressively more TKE is produced, in the early stage it resides predominantly in streamwise fluctuations, promoting a more one-dimensional turbulence. A rapid recovery of wall-normal and spanwise pressure strain terms signifies the onset of retransition. In comparison, the small-span case matches very well the development of $P_{s,11}$ and the initial decrease of pressure strain terms. However, the recovery of pressure strain terms during the retransition is significantly slower.

Structural characteristics are also compared. The two-point velocity auto-correlation R_{uu} with separation r_{x_i} in x_i direction is defined as

$$R_{uu}(r_x, r_y) = \langle \overline{u'(x, y_{\rm ref}, z, t)u'(x + r_x, y_{\rm ref} + r_y, z, t)} \rangle / \langle \overline{u'^2} \rangle (y_{\rm ref}), \tag{3.5}$$

where $y_{\rm ref}$ is the elevation at which R_{uu} is centered. Figure 9(a,b) show the variation of isocontour of $R_{uu}(r_x, r_y) = 0.3$ centered at an elevation near the wall throughout the transient. For the full-span case, This elevation is chosen at $y/\delta_{\nu 1} = 15$ (Figure 9(a)) and $y/\delta_{\nu 2} = 15$ (Figure 9(b)) for the discussion of the reverse-transition and retransition processes, respectively. Times shown include $t^* = 0$ (initial equilibrium state), 0.5 (reverse-transition), 0.6 and 0.7 (around the onset of retransition), 1.0 (during retransition) and 1.5 (new equilibrium state). The near-wall large-scale u' motions are elongated in x during the reverse-transition stage and are progressively shortened during the retransition.

Figure 9(c) compares the temporal variation of the streamwise extents of the isocontour of $R_{uu} = 0.3$ centered at $y/\delta_{\nu 1} = 15$, between the two cases. The overall variation of R_{uu} is well captured by the small-span simulations, except for a delayed onset of reduced streamwise coherence in the retransition process.

Figure 10 shows the 2D premultiplied power spectra of u', $\kappa_1\kappa_3\langle\overline{|\hat{u}\hat{u}^*|}\rangle$ (normalized by δ and $u_{\tau 1}$), at $y/\delta_{\nu 1} = 15$. Here, κ_i and λ_i are the wavenumber and wavelength in x_i direction, $\hat{u}$ is the Fourier transform of u', and $*$ indicates complex conjugate. During the reverse transition, the peak location of the power spectrum shifts toward a larger λ_1, indicating a higher fraction of total energy residing in motions with very large x extents, while the z extent of these motions are not affected. This phenomenon continues well into the retransition phase, despite the growth of energy residing in much smaller motions associated with the higher Reynolds number. The very-large-wavelength spectral peak disappears later (at $t^* \approx 1$), accompanied by a shift of σ_u peak elevation toward the

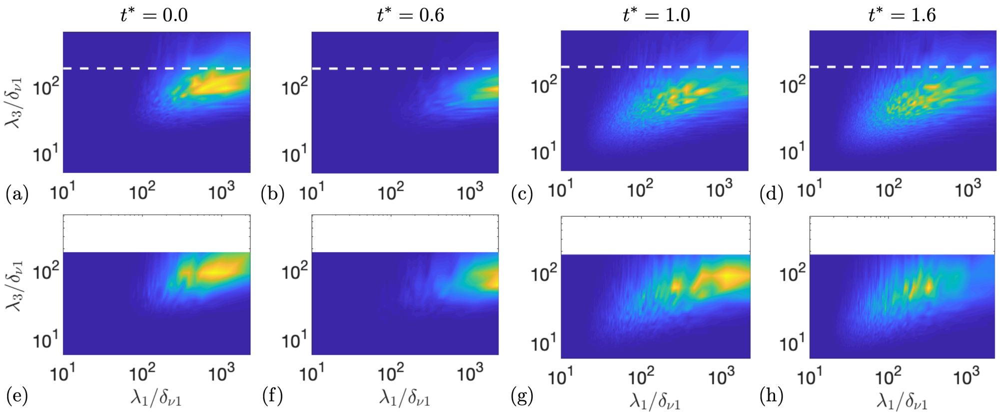

FIGURE 10. Premultiplied power spectra of u' at $y/\delta_{\nu1} = 15$ for full- (a-d) and small-span (e-h) smooth cases, normalized using u_{b1} and δ. --- L_z of small-span case.

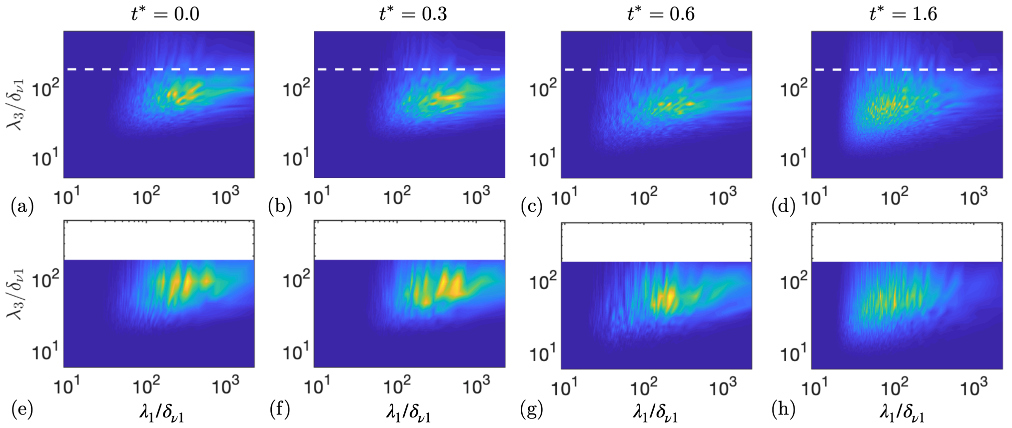

FIGURE 11. Premultiplied power spectra of v' at $y/\delta_{\nu1} = 30$ for full- (a-d) and small-span (e-h) smooth cases, normalized using u_{b1} and δ. --- L_z of small-span case.

new elevation in the new equilibrium state as shown in Figure 7(b). The above variations are well captured by the small-span case, except for a delay in the shift of the spectral maxima toward smaller scales during retransition.

Figure 11 and Figure 12 show the 2D power spectra of v' and w', respectively, with the same normalization as in Figure 10. A higher elevation of $y/\delta_{\nu1} = 30$ is evaluated, as it is close to the peak elevations of v' and w'. Initially, the v' and w' power spectra undergo a right shift of the spectral peak similar to u' spectra, but their peaks shift to smaller scales at the end of reverse-transition stage ($t^* \approx 0.6$), much earlier than u' motions, and the equilibrium state recovers much earlier. It is because most of the v' and w' energy resides in turbulent spots at the start of the retransition. Throughout the transient, the small span captures the majority of the energetic scales of v' motions. This, however, is not the case for w' motions. Figure 12(a-d) shows that a major portion of the near-wall large-z-scale ($\lambda_3/\delta_{\nu1} > 180$) w' energy is not captured by L_z in the small span simulation, which explains the previous observation of underestimated span-wise fluctuations throughout the transient (in Figure 2, 7).

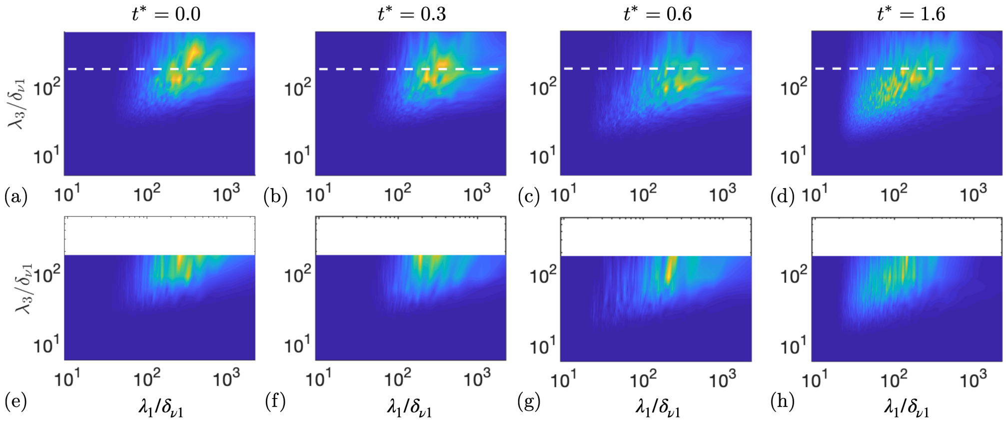

FIGURE 12. Premultiplied power spectra of w' at $y/\delta_{\nu 1} = 30$ for full- (a-d) and small-span (e-h) smooth cases, normalized using u_{b1} and δ. - - - L_z of small-span case.

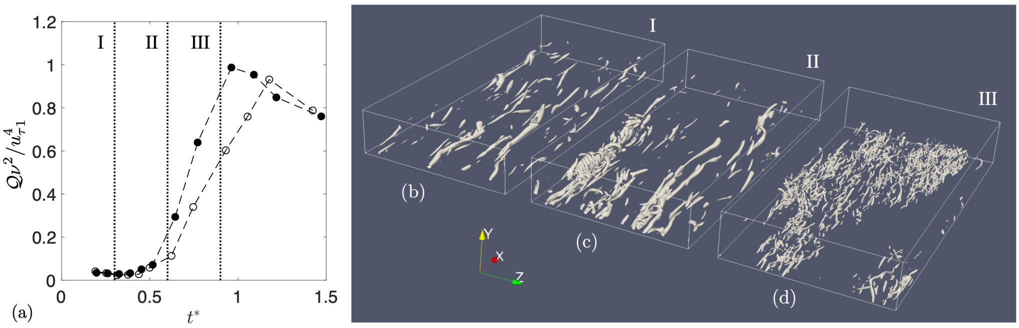

FIGURE 13. (a) Measure of strength of quasi-streamwise vortices using $\mathcal{Q}(t)$ defined in Equation (3.6) for full- (filled symbols) and small-span (open symbols) smooth cases. Isosurfaces of $Q\delta^2/u_{b1}^2 = 3$ for $t^* = 0.3$ (reverse-transition, (b)), 0.6 (onset of retransition, (c)) and isosurface of $Q\delta^2/u_{b1}^2 = 90$ for $t^* = 0.9$ (retransition, (d)), in the full-span case. The three t^* instances are marked in (a).

3.2.2. *Effect of a small span in near-wall dynamics*

We now explain the differences observed previously. The near-wall turbulence production cycle involves the interaction between low-speed streaks and quasi-streamwise vortices (Hamilton *et al.* 1995; Hwang & Bengana 2016; Schoppa & Hussain 2002; Jiménez & Pinelli 1999*b*). Previous studies proposed that: (1) quasi-streamwise vortices lead to the lift-up of streaks through $\omega_x(\partial u'/\partial y)$; and (2) the streaks (which meander in the streamwise direction) in turn contribute to the generation of quasi-streamwise vortices through vortex stretching and wall-normal advection. Here, we explore what happens to this cycle during the transient and how a small span affects the change.

Figure 13(b-d) show the temporal evolution of vortical motions in case SF, visualized as iso-surfaces of the second invariant of the velocity gradient tensor, $Q = -u_{i,j}u_{j,i}/2$. In the reverse-transition phase (demonstrated by state I), the quasi-streamwise vortices are elongated and are fewer compared to the initial equilibrium state. At the onset of retransition (near state II), smaller-scaled vortical motions appear and grow during the retransition (state III).

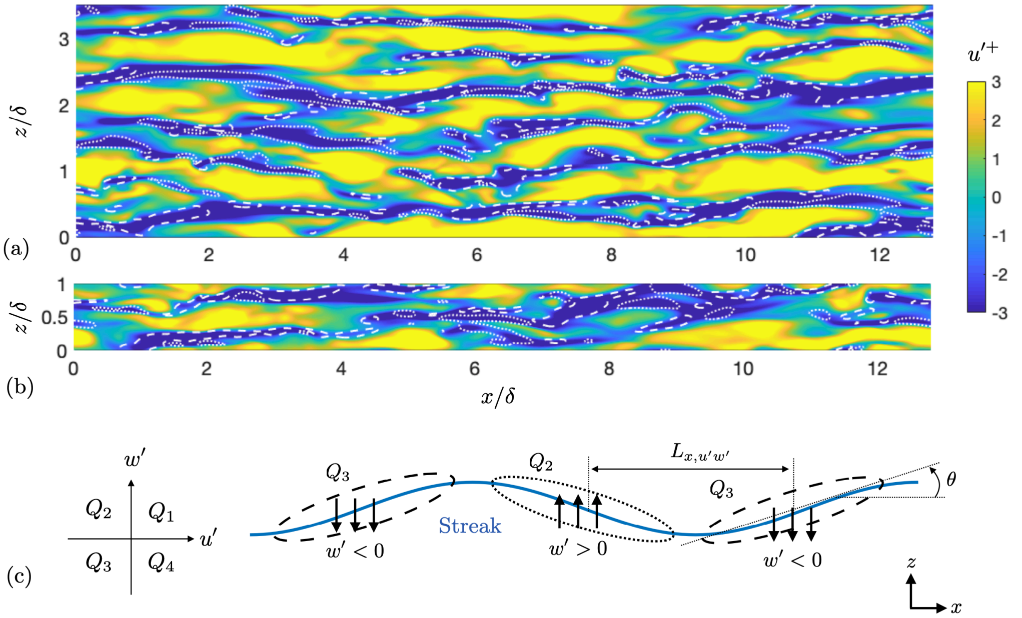

FIGURE 14. Visualization of near-wall low-speed streaks for (a) full- and (b) small-span smooth cases at $y^+ = 15$ and $t^* = 0$. – – – $(u'w')^+|_{Q3} = 1.5$, ··· $(u'w')^+|_{Q2} = -1.5$. (c) Sketch of distribution of $u'w'$ quadrants along a meandering streak.

The strength of quasi-streamwise vortices can be measured using the volume-averaged instantaneous Q conditioned on an x-aligned vortical axis (identified using $\omega_x^2/|\vec{\omega}|^2 > 0.8$, where $\vec{\omega}$ is the fluctuation vorticity) and positive values of Q. This conditional average is denoted as $\mathcal{Q}$,

$$\mathcal{Q}(t) = \frac{1}{\mathcal{V}_n} \int_{\mathcal{V}_n} \overline{Q(\vec{x}, t)|_{\omega_x^2/|\vec{\omega}|^2 > 0.8; Q>0}} \, \mathrm{d}x \mathrm{d}y \mathrm{d}z, \tag{3.6}$$

where the averaging volume $\mathcal{V}_n$ is the the volume of the near-wall layer below the peak elevation of the ω_x rms at each time instance. $\mathcal{V}_n$ varies in time. Such a dynamically adapting averaging volume is used to ensure that the vortical motions contributing to $\mathcal{Q}$ are indeed predominantly quasi-streamwise vortices, as well as to dynamically adjust to the variation of viscous sublayer thickness in time. $\mathcal{Q}$ is compared in Figure 13(a) between cases SF and SS. Both cases display roughly constant vorticity strength during reverse transition and a rapid augmentation of the intensity during retransition, attributed to the generation of smaller-scale new turbulence through the near-wall cycle. A significant delay in the augmentation of the strength of quasi-streamwise vortices is seen for the small-span case.

Next, we attribute the delay of the recovery of turbulent statistics and structure in the small-span simulation to a weaker streak transient growth phenomenon. Other mechanisms may also contribute to the delay but are beyond the scope of this work.

Schoppa & Hussain (2002) showed that a streak transient growth (STG) mechanism dominates generation of near-wall quasi-streamwise vortices for canonical wall-bounded turbulence. Such mechanics arises from the streamwise variation of w' perturbations, with the second and third quadrants (Q2 and Q3) of $u'w'$ events being a critical trigger for turbulence production. Figure 14(a,b) displays the near-wall low-speed streaks for full-

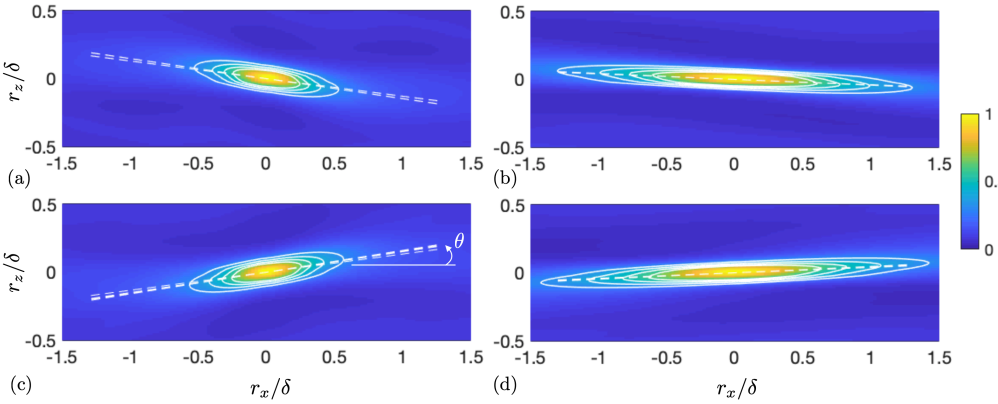

FIGURE 15. Two-point auto-correlations of Q2 (a-b) and Q3 (c-d) contributions to $u'w'$ at $y^+ = 15$ and $t^* = 0$ (a,c) and 0.3 (b,d), for the full-span smooth case. Contour levels are from 0.3 to 0.6 with step size 0.1; - - - principal axis of a contour line. r_{x_i} is separation in x_i.

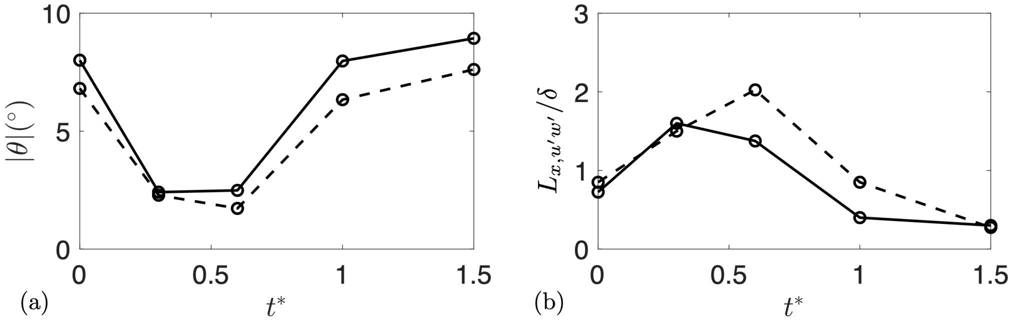

FIGURE 16. Characteristics of streak meandering at $y^+ = 15$: (a) average tilting angle magnitude and (b) average streamwise separation between alternating Q2 and Q3 regions, for full- (———) and small-span (- - -) smooth cases.

and small-span cases at $y^+ = 15$ and $t^* = 0$, superimposed by isocontour lines of Q2 and Q3 quadrants of $u'w'$. An association of the distribution of these quadrant events with streak meandering is clear; this is due to the spatial organization of low-speed streaks and quasi-streamwise vortices (Jeong *et al.* 1997; Schoppa & Hussain 2002). Similar observations was made also by Schoppa & Hussain (2002). We verified that a variation of y^+ locations between 5 and 25 does not affect the general pattern shown. According to the STG mechanism of quasi-streamwise vorticity generation (Schoppa & Hussain 2002), the spanwise meandering of a low-speed streak is due to the convection of the streak by x-dependent w' perturbations and, in turn, generates ω_x through vortex stretching by $\partial u/\partial x$ as a result of the meandering. Different levels of meandering would thus indicate different generation rates of quasi-streamwise vortices.

To quantitatively compare the characteristics of the meandering of low-speed streaks in cases SS and SF, we calculate, for each case at various t^*: (1) the average tilting angle θ (in $x - z$ plane) of the Q2 and Q3 regions, representing meandering magnitude; and (2) the average separation between x-alternating Q2 and Q3 events $L_{x,u'w'}$, representing (a half of) the meandering wavelength. These two variables are sketched in Figure 14(c).

To calculate θ and $L_{x,u'w'}$, the two-dimensional auto-correlations (with separation in

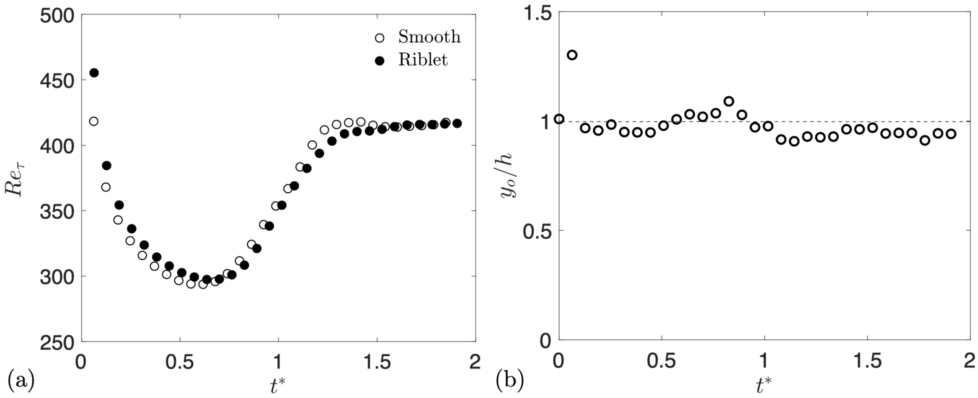

FIGURE 17. (a) Variations of Re_τ with time for smooth (empty symbols) and riblet (filled symbols) cases. (b) Variation of virtual origin y_o defined in Equation (3.7) with time. - - - $y_o/h = 1$.

x and z) of $u'w'$ in Q2 and Q3 quadrants are obtained for each t^*; they are compared at $t^* = 0$ and 0.3 in Figure 15. The tilting directions are consistent with the visualization and sketch in Figure 14. The principal axes of each contour level is obtained based on principal component analysis. θ is obtained as the tilting angle of the long axis of a contour line with respect to x; this angle is then averaged among values obtained from contour levels from 0.3 to 0.6 with a step size of 0.1. Next, the two-point cross-correlation of Q2 and Q3 events with separation in x are calculated at $y^+ = 15$ for each t^*. we define $L_{x,u'w'}$ as the x separation associated with the maximum correlation magnitude, roughly representing the average separation between the centers of neighboring Q2 and Q3 regions.

The values of θ and $L_{x,u'w'}$ at representative values of t^* are compared in Figure 16. In both cases, the angle of meandering decreases during reverse transition and recovers during retransition. At the same time, the wavelength of meandering first increases then decreases to the new equilibrium value. It indicates a stabilization of streaks with significantly milder meandering both in terms of lower magnitudes and longer wavelengths during reverse transition. Noticeable differences are seen between the two cases. Before the transient (at $t^* = 0$) the full-span case yields a significantly higher meandering magnitude but a similar wavelength—probably a result of the missing w' motions with large λ_z and broad-band λ_x in the small-span case (shown by Figure 12(a,e)). The weaker meandering angle in case SS continues to the onset of retransition ($t^* \approx 0.6$), and, through a weaker STG mechanism, tends to generate fewer or weaker quasi-streamwise vortices. Thus slower turbulence generation and retransition processes follow. A change of y^+ between 5 and 25 does not affect the overall comparison, despite that the value of θ varies with y^+. We conclude that the small-span simulations capture the variation of essential near-wall dynamics for turbulence generation in a transient, accelerating flow, though quantitative differences in the speed of flow recovery remain due to large-z-scale w' motions that are not captured.

3.3. *Transient flow over Riblets*

In this section, the effect of riblets on statistics and dynamics will be described by comparing cases SS and RS. As one will see, the overall dynamics of turbulent flow during the transient is not modified by riblets; this is shown by similar time-variations of the wall friction, the mean velocity profiles, the Reynolds stresses and characteristics of streak meandering, as compared to the smooth-wall case. The main effect of riblets appears to be a reduction of streak meandering and consequently a delay of the start of the retransition process due to a slower streak-transient growth.

First, Figure 17(a) compares the variation of $Re_\tau(t)$. The main differences include a slight delay in the onset of retransition and a lack of overshoot for the riblet case. Previously, the experimental study of Grek *et al.* (1996) showed that the presence of riblets delayed the formation of turbulence spots in the laminar-to-turbulent transition in a boundary layer. The parametric study of He & Seddighi (2015) for flow configurations similar to this work showed that a lower initial turbulence intensity delays the onset of retransition, reminiscent of the dependence of the critical Reynolds number for a by-pass transition in a boundary-layer flow on the freestream turbulence. Similarly, the delay of retransition in the present riblet case is probably due to a lower initial turbulence intensity. At $t^* = 0$, the peak values of the y profiles of $\sigma_{u_i}/u_{\tau 2}$ are 2%, 5% and 3%, for u', v' and w' components respectively, lower than the values in the smooth case.

Another observation from Figure 17(a) is that, early in the transient, Re_τ is higher on the riblets than on the smooth wall. Given that the Reynolds shear stress is roughly 7% lower for the riblet case at this time (in peak value, shown later in Figure 20), a plausible explanation may be that the higher surface area on the riblet surface leads to higher total viscous shear stress early in the transient.

To compare the flow statistics between cases with or without riblets, one needs to quantify the virtual y origin for case RS to align the logarithmic region (if present) between the two cases. Various definitions of the virtual origin were used in the literature, including but not limited to the riblet tip elevation, valley elevation, and the midpoint between the two. Here, we compare two definitions. The first is the midpoint between the tip and valley, $y = 0.5h$. The second, denoted as y_o, is an extension from the definition used by Choi *et al.* (1993) for equilibrium flows. Here, y_o is defined dynamically such that the elevations of maximum u' rms in the cases with and without riblets are aligned on the y^+ axis offset by y_o, at any given time. In other words,

$$y_o(t) = y_{\max}(t) - \frac{y^+_{\max,SS}(t)\nu}{u_\tau(t)}. \tag{3.7}$$

Here, $y_{\max}$ is the peak elevation of σ_u in any of the two cases, $y^+_{\max,SS}$ is the y^+ value corresponding to the σ_u peak in case SS. The reason for this definition is that the logarithmic region is closely related to the region of balance between the TKE production and dissipation, which moves upward during the transient flow due to the thickening of the viscous sublayer. By matching the peak elevation of u' rms—which is also the peak location of TKE production—the definition in Equation (3.7) thereby aligns the logarithmic regions on the offset y^+ axis. For case SS, $y_o = 0$, while for case RS Figure 17(b) shows the variation of y_o/h. It is evident that the virtual origin defined in Equation (3.7) lies in the vicinity of the riblet tip during most of the transient process, except immediately after the u_b step jump.

Figure 18 compares the variation of U against the y offset by the virtual origin, defined either in Equation (3.7) or as $0.5h$. Regardless of the virtual origin definition, the change of profile shape in the riblet case is similar to that of a smooth wall, with a thickening of the linear velocity region, a increase of log-law intercept and a slight decrease of log-law slope. The difference of the U values in the logarithmic region in the riblet case from the smooth-wall profile ($\Delta U^+ = U^+_{SS} - U^+_{RS}$), however, depends slightly on the virtual origin definition used. Specifically, the upper shift of U^+ (or $\Delta U^+ < 0$) representing the

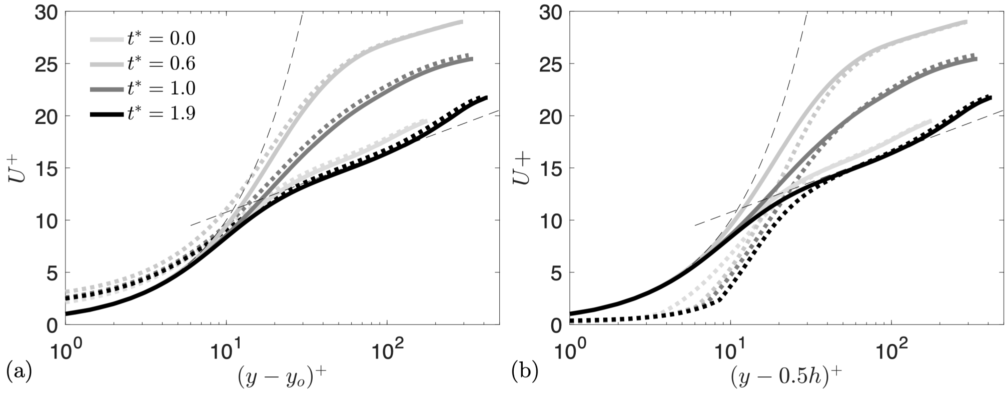

FIGURE 18. Double-averaged velocity for smooth (——) and riblet (- - -) cases, with y shifted by (a) y_o defined in Equation (3.7) and (b) mean height ($0.5h$).

drag-reduction effect of riblets in the equilibrium states is less when using the offset of $0.5h$.

Next, the effect of the riblet on the drag during the transient is analyzed. We use ΔU^+ in the logarithmic region to quantify the change of drag as it is independent from the shape of outer-layer U profile. It is noted that, in previous studies of equilibrium flows on riblets, the drag reduction is often quantified differently, as the relative difference in the friction coefficient between two cases at the same Re_τ, i.e. $1 - C_{f,r}/C_{f,s} \approx \sqrt{2C_{f,s}}(U^+_{c,s} - U^+_{c,r})$ (Spalart & McLean 2011), where C_f is the friction coefficient, U_c is the centerline velocity of the channel, and subscripts "r" and "s" represent riblet and smooth-wall cases. Such quantification, however, requires knowledge of the ratio of u_τ/U_c, which is not available herein due to the overpredicted value of U_c obtained from the small spanwise domain size. Second, this definition of drag reduction assumes that the U profile shape far from the wall is similar between the riblet and the smooth-wall cases. In non-equilibrium flows, however, the U^+ profile shape undergoes significant changes over time and this assumption may not apply. Third, Re_τ values are not matched for both cases for all time. For these reasons, we use ΔU^+, instead of $1 - C_{f,r}/C_{f,s}$, to quantify the drag change due to riblets. Another advantage of using ΔU^+ is that it is not Reynolds number dependent.

To identify the logarithmic region in a non-equilibrium flow, we use a diagnostic function based on the U^+ profile following Spalart (1988), $\Xi(y) = (y - y_o)^+ \partial U^+ / \partial y^+$. Figure 19(a) compares Ξ at representative t^* instances of 0.0 (initial steady state), 0.3 (reverse transition), 0.6 (onset of retransition), and 1.9 (final steady state). The logarithmic region, when it exists, would be located between two bounds: (1) $(y - y_o)^+ = 30$, considered as the upper limit of the buffer layer; and (2) $y/\delta = 0.35$, considered as the lower limit of the outer layer. A plateau region or a local minima of Ξ is observed for the two steady states and for $t^* = 0.3$, indicating the existence of logarithmic profiles at these times. The location and the logarithmic slope (obtained as the Ξ value in the logarithmic region) appear to match roughly for these two cases. For t^* in the range of 0.4 to 1.1, the logarithmic region does not exist for either flow, as shown in Figure 19(a) at $t^* = 0.6$.

Figure 19(b) shows the variation of ΔU^+ in the t^* range for which a logarithmic layer is present. The t^* duration between 0.4 and 1.1 is blocked out to indicate the absence of the logarithmic profile and, consequently, an ill-defined ΔU^+. It is shown that the

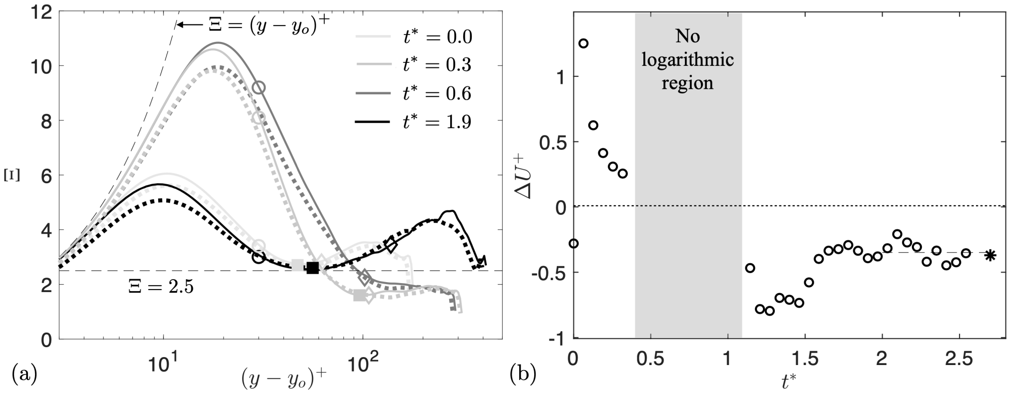

FIGURE 19. (a) Diagnostic function, $(y - y_o)^+ \partial U^+/\partial y^+$, for smooth (——) and riblet (···) cases, compared with law-of-the-wall (- - -) in equilibrium flows. Filled squares: elevation of logarithmic region (if present); ○ $y^+ = 30$; ◇ $y/\delta = 0.35$. (b) Drag change due to riblets. - - - ΔU^+ in new equilibrium; $*$ Bechert *et al.* (1997) experiment.

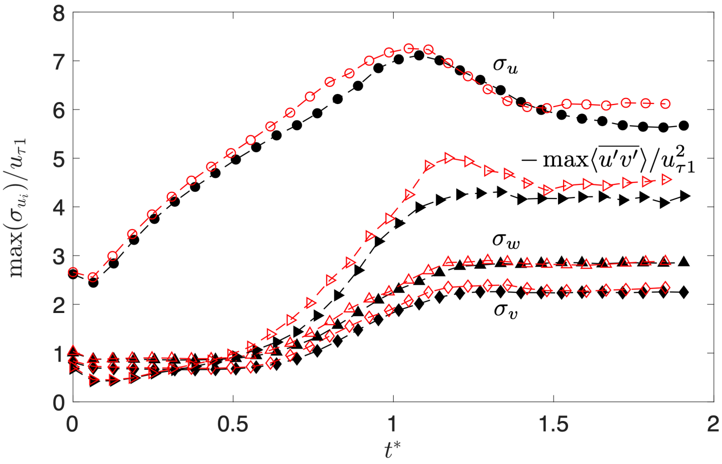

FIGURE 20. Temporal variations of peak values of velocity rms fluctuations and Reynolds shear stress, normalized by initial u_τ, for smooth (open symbols) and riblet (filled symbols) cases.

riblets increase the drag in the reverse-transition phase, while decreasing the drag in the retransition phase. This is in part due to the higher viscous stress early in the reverse-transition phase and also in some degree due to the delayed response of wall friction in the reverse-transition phase, as shown in Figure 17(a). In the final equilibrium state the riblet is drag-reducing (by design), with a ΔU^+ comparing well with the drag-reduction measurement by Bechert *et al.* (1997) (converted to ΔU^+ by MacDonald *et al.* (2017*a*) based on the assumption of an equilibrium flow) for matching riblet geometry, Re_τ and h^+.

The Reynolds stress profiles in the riblet case take similar shapes to those over a smooth wall. To quantitatively compare them, Figure 20 shows the variation of the peak values of rms fluctuations and Reynold shear stress for both cases, normalized by the initial u_τ. One difference is the lower σ_u peak magnitude on riblets in both the initial

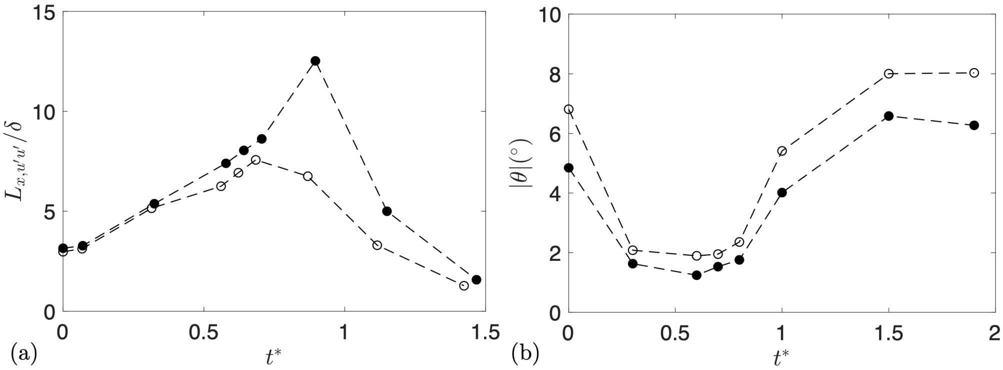

FIGURE 21. Temporal variations of (a) x extent of $R_{uu} = 0.3$ isocontour centered at $y/\delta_{\nu 1} = 15$ and (b) average streak tilting angle magnitude (calculated at $y/\delta_{\nu 1} = 15$), for smooth (open symbols) and riblet (filled symbols) cases.

and final equilibrium states, as well as before the retransition. The σ_v peak magnitude is also noticeably lower on riblets throughout the transient, yielding a weaker Reynolds shear stress as a consequence. For equilibrium flows, it has typically been observed that drag-reducing riblets lead to reduced fluctuation magnitudes. Here we show that it is also true for strongly accelerating flows.

To compare the characteristics of streaks between the two cases, the x extent of the R_{uu} isocontour ($L_{x,u'u'}$) is shown in Figure 21(a). $L_{x,u'u'}$ is calculated from $R_{uu}(r_x, r_y)$ centered at $y/\delta_{\nu 1} = 15$. Although the elongation of low-speed streaks during the riblet-flow reverse-transition phase and smooth cases are similar, such elongation lasts significantly longer in the presence of riblets (with the onset of streak breakdown at $t^* \approx 0.9$, a 0.2 delay from the smooth case). Figure 21(b) shows that throughout the transient the mean streak tilting angle, $|\theta|$, is consistently 25% to 30% lower in the riblet case. The experimental visualizations of Bacher & Smith (1985) also showed that drag-reducing riblets attenuate streak oscillation for a ZPG boundary layer. A weaker streak meandering, together with a slightly weaker w' magnitude, suggests that weaker or fewer quasi-streamwise vortices are generated for all t^* through the STG mechanism and consequently the retransition is delayed. Longer u' correlation lengths and lower turbulence intensities during the transient appear to be manifestations of such a delayed response.

Conclusions

Direct numerical simulations of turbulent half channel flows subjected to a step increase of the bulk velocity are carried out on a smooth wall with different spanwise domain sizes to evaluate simulations of non-equilibrium, strongly accelerating turbulence with the minimal-span methodology. Comparison is made with a base case with a full span. Following the impulse acceleration, the near-wall cycle of turbulence generation is modified due to increased stability of streaks. TKE steadily increases, while reverse transition toward a quasi-laminar state occurs with a decrease of Re_τ and elongated low-speed streaks, as the pressure-strain term of Reynolds stress budgets redistributes most of the TKE to streamwise fluctuations. The flow then retransitions toward the final equilibrium state as turbulent spots appear and the normal near-wall cycle of turbulence generation resumes.

The small-span case captures the variation in turbulence statistics and structure, while displaying a more persistent stabilized turbulence during the transient and a delayed establishment of the new equilibrium state. A candidate mechanism underlying this different is linked to the missing near-wall w' motions that are large-scale in z and broadband in x, due to the exclusion of large attached eddies by the limited span. These missing w' motions may explain the milder streak meandering, which is then associated with a weaker streak-transient-growth mechanism that is important in generation of quasi-streamwise vortices. A slower intensification in overall vortical strength of x-aligned vortical motions is indeed observed and eventually leads to a later onset of streak destabilization at the start of the retransition.

Having shown that the small span captures the essential near-wall physics (despite quantitative differences) in this type of non-equilibrium flows, we apply the small-span simulation in characterizing the effects of wall riblets (drag-reducing in equilibrium states) in non-equilibrium, accelerating transient channel. Results are compared to the small-span smooth-wall data. The location of the virtual origin defined based on the dynamic argument (Choi *et al.* 1993) is shown consistently around the riblet tip throughout the transient. In addition, the riblets weaken the turbulence intensity at all time, similar to past observations on fully-developed flows. The presence of riblets does not fundamentally alter the dynamics. The main difference is a delayed onset of retransition and delayed flow recovery which may, again, be due to weaker streak transient growth, as the streak meandering (quantified by the mean tilting angle) is significantly milder than the smooth case at all time. Interestingly, instantaneous comparison with the smooth case shows that the riblets are drag-increasing during the reverse transition; this may be due partially to the larger wetted area of the riblets which yields larger amount of viscous drag. In the retransition stage, however, the riblets are drag-reducing, partially due to the later retransition onset.

These results provide confidence in the use of small-span simulations for extraction of main physics in a wall turbulence subject to a strong acceleration of the bulk flow. Also as discussed in section 2.3, high spanwise resolution is required to resolve riblet's profile and several transient simulations are needed for ensemble averaging, which reflects on the cost-effectiveness of this approach. And using this approach, we showed that previously observed streak-stabilization effect of riblets in fully-developed wall turbulence is still present when the flow is strongly accelerating and serves to prolong the transient process by delaying the retransition.

REFERENCES

Bacher, E. v. & Smith, C. 1985 A combined visualization-anemometry study of the turbulent drag reducing mechanisms of triangular micro-groove surface modifications. In *Shear Flow Control Conference*, p. 548.

Bechert, D. & Bartenwerfer, M. 1989 The viscous flow on surfaces with longitudinal ribs. *J. Fluid Mech.* **206**, 105–129.

Bechert, D., Bruse, M., Hage, W. v., Van der Hoeven, J. T. & Hoppe, G. 1997 Experiments on drag-reducing surfaces and their optimization with an adjustable geometry. *J. Fluid Mech.* **338**, 59–87.

Bourassa, C. & Thomas, F. 2009 An experimental investigation of a highly accelerated turbulent boundary layer. *J. Fluid Mech.* **634**, 359–404.

Brereton, G. 2000 The interdependence of friction, pressure gradient, and flow rate in unsteady laminar parallel flows. *Phys. Fluids* **12** (3), 518–530.

Choi, H., Moin, P. & Kim, J. 1993 Direct numerical simulation of turbulent flow over riblets. *J. Fluid Mech.* **255**, 503–539.

Chung, D., Chan, L., MacDonald, M., Hutchins, N. & Ooi, A. 2015 A fast direct numerical simulation method for characterising hydraulic roughness. *J. Fluid Mech.* **773**, 418–431.

Dean, B. & Bhushan, B. 2010 Shark-skin surfaces for fluid-drag reduction in turbulent flow: a review. *Philos. T. R. Soc. A* **368** (1929), 4775–4806.

Flores, O. & Jiménez, J. 2010 Hierarchy of minimal flow units in the logarithmic layer. *Phys. Fluids* **22** (7), 071704.

García-Mayoral, R. & Jiménez, J. 2011 Drag reduction by riblets. *Philos. T. R. Soc. A* **369** (1940), 1412–1427.

GEC, A. 1991 Industrial applications of drag reduction to the French high speed trains (TGV). In *6th European drag reduction meeting, Eindhoven*, pp. 21–22.

Goldstein, D., Handler, R. & Sirovich, L. 1995 Direct numerical simulation of turbulent flow over a modeled riblet covered surface. *J. Fluid Mech.* **302**, 333–376.

Goldstein, D. B. & Tuan, T.-C. 1998 Secondary flow induced by riblets. *J. Fluid Mech.* **363**, 115–151.

Grek, G., Kozlov, V. & Titarenko, S. 1996 An experimental study of the influence of riblets on transition. *J. Fluid Mech.* **315**, 31–49.

Hamilton, J. M., Kim, J. & Waleffe, F. 1995 Regeneration mechanisms of near-wall turbulence structures. *J. Fluid Mech.* **287**, 317–348.

He, S. & Seddighi, M. 2013 Turbulence in transient channel flow. *J. Fluid Mech.* **715**, 60–102.

He, S. & Seddighi, M. 2015 Transition of transient channel flow after a change in Reynolds number. *J. Fluid Mech.* **764**, 395–427.

Hwang, Y. 2013 Near-wall turbulent fluctuations in the absence of wide outer motions. *J. Fluid Mech.* **723**, 264–288.

Hwang, Y. 2015 Statistical structure of self-sustaining attached eddies in turbulent channel flow. *J. Fluid Mech.* **767**, 254–289.

Hwang, Y. & Bengana, Y. 2016 Self-sustaining process of minimal attached eddies in turbulent channel flow. *J. Fluid Mech.* **795**, 708–738.

Jeong, J., Hussain, F., Schoppa, W. & Kim, J. 1997 Coherent structures near the wall in a turbulent channel flow. *J. Fluid Mech.* **332**, 185–214.

Jiménez, J. & Pinelli, A. 1999*a* The autonomous cycle of near-wall turbulence. *J. Fluid Mech.* **389**, 335–359.

Jiménez, J. & Pinelli, A. 1999*b* The autonomous cycle of near-wall turbulence. *J. Fluid Mech.* **389**, 335–359.

Keating, A., Piomelli, U., Bremhorst, K. & Nesic, S. 2004 Large-eddy simulation of heat transfer downstream of a backward-facing step. *J. Turbul.* **5** (20), 1–3.

Kim, J., Moin, P. & Moser, R. D. 1987 Turbulence statistics in fully developed channel flow at low Reynolds number. *J. Fluid Mech.* **177**, 133–166.

Krieger, K. 2004 Do pool sharks swim faster?

Launder, B. 1964 Laminarization of the turbulent boundary layer in a severe acceleration. *J. Appl. Mech.* **31** (4), 707–708.

LEE, S.-J. & CHOI, Y.-S. 2008 Decrement of spanwise vortices by a drag-reducing riblet surface. *J. Turbul.* (9), N23.

LEE, S.-J. & JANG, Y.-G. 2005 Control of flow around a NACA 0012 airfoil with a micro-riblet film. *J. Fluid Struct.* **20** (5), 659–672.

LUCHINI, P., MANZO, F. & POZZI, A. 1991 Resistance of a grooved surface to parallel flow and cross-flow. *J. Fluid Mech.* **228**, 87–109.

MACDONALD, M., CHUNG, D., HUTCHINS, N., CHAN, L., OOI, A. & GARCÍA-MAYORAL, R. 2017*a* The minimal-span channel for rough-wall turbulent flows. *J. Fluid Mech.* **816**, 5–42.

MACDONALD, M., CHUNG, D., HUTCHINS, N. & OOI, A. 2017*b* Predicting the performance of riblets in a minimal cahnnel. In *European Drag Reduction and Flow Control Meeting – EDRFCM*.

MCELIGOT, D. M. & ECKELMANN, H. 2006 Laterally converging duct flows. Part 3. Mean turbulence structure in the viscous layer. *J. Fluid Mech.* **549**, 25–59.

MCLEAN, J., GEORGE-FALVY, D. & SULLIVAN, P. 1987 Flight-test of turbulent skin-friction reduction by riblets. *Turbulent drag reduction by passive means* pp. 408–424.

NARASIMHA, R. & SREENIVASAN, K. 1973 Relaminarization in highly accelerated turbulent boundary layers. *J. Fluid Mech.* **61** (3), 417–447.

NIKORA, V., MCEWAN, I., MCLEAN, S., COLEMAN, S., POKRAJAC, D. & WALTERS, R. 2007 Double-averaging concept for rough-bed open-channel and overland flows: Theoretical background. *J. Hydraul. Eng.* **133** (8), 873–883.

PIOMELLI, U. & YUAN, J. 2013 Numerical simulations of spatially developing, accelerating boundary layers. *Phys. Fluids* **25** (10), 101304.

RAJU, C. & VISWANATH, P. 1998 Base drag reduction caused by riblets on a gaw (2) airfoil. *J. Aircraft* **35** (6), 988–991.

RASTEGARI, A. & AKHAVAN, R. 2019 On drag reduction scaling and sustainability bounds of superhydrophobic surfaces in high Reynolds number turbulent flows. *J. Fluid Mech.* **864**, 327–347.

RAUPACH, M. R. & SHAW, R. 1982 Averaging procedures for flow within vegetation canopies. *Bound.-Lay. Meteorol.* **22** (1), 79–90.

SCHOPPA, W. & HUSSAIN, F. 2002 Coherent structure generation in near-wall turbulence. *J. Fluid Mech.* **453**, 57–108.

SEDDIGHI, M., HE, S., POKRAJAC, D., O'DONOGHUE, T. & VARDY, A. E. 2015 Turbulence in a transient channel flow with a wall of pyramid roughness. *J. Fluid Mech.* **781**, 226–260.

SMITH, C. R., WALKER, J. D. A., HAIDARI, A. H. & TAYLOR, B. K. 1990 Hairpin vortices in turbulent boundary layers: the implications for reducing surface drag. In *Structure of Turbulence and Drag Reduction*, pp. 51–58. Spirnger, Berlin, Heidelberg.

SPALART, P. R. 1988 Direct simulation of a turbulent boundary layer up to $R_\theta = 1410$. *J. Fluid Mech.* **187**, 61–98.

SPALART, P. R. & MCLEAN, J. D. 2011 Drag reduction: enticing turbulence, and then an industry. *Philos. T. R. Soc. A* **369** (1940), 1556–1569.

SZODRUCH, J. 1991 Viscous drag reduction on transport aircraft. In *29th Aerospace Sciences Meeting*, p. 685.

WALSH, M. J. 1983 Riblets as a viscous drag reduction technique. *AIAA journal* **21** (4), 485–486.

WEISS, M. H. 1993 *Drag reduction with riblets in pipe flow*. University of Calgary.

Yuan, J. & Piomelli, U. 2014*a* Numerical simulations of sink-flow boundary layers over rough surfaces. *Phys. Fluids* **26** (1), 015113.

Yuan, J. & Piomelli, U. 2014*b* Roughness effects on the reynolds stress budgets in near-wall turbulence. *J. Fluid Mech.* **760**, R1.

Yuan, J. & Piomelli, U. 2015 Numerical simulation of a spatially developing accelerating boundary layer over roughness. *J. Fluid Mech.* **780**, 192–214.